



## Photoinduced composite of Pt decorated Ni(OH)<sub>2</sub> as strongly synergistic cocatalyst to boost H<sub>2</sub>O activation for photocatalytic overall water splitting

Shangcong Sun<sup>a,b</sup>, Yong-Chao Zhang<sup>a,b</sup>, Guoqiang Shen<sup>a,b</sup>, Yutong Wang<sup>a,b</sup>, Xianlong Liu<sup>a</sup>, Zhenwei Duan<sup>a</sup>, Lun Pan<sup>a,b</sup>, Xiangwen Zhang<sup>a,b</sup>, Ji-Jun Zou<sup>a,b,\*</sup>

<sup>a</sup> Key Laboratory for Green Chemical Technology of the Ministry of Education, School of Chemical Engineering and Technology, Tianjin University, Tianjin, 300072, China

<sup>b</sup> Collaborative Innovative Center of Chemical Science and Engineering (Tianjin), Tianjin, 300072, China



### ARTICLE INFO

#### Keywords:

Photocatalysis  
Water splitting  
H<sub>2</sub>O activation  
Cocatalyst

### ABSTRACT

Photocatalytic overall water splitting is one of the ultimate goals in solar conversion and the activation and cleavage of H<sub>2</sub>O molecule is the initial and often rate-determining step in this reaction. Through DFT calculations, we designed Pt cluster decorated Ni(OH)<sub>2</sub> nanoparticles (Pt/Ni(OH)<sub>2</sub>) as robust cocatalyst capable of activating H<sub>2</sub>O and dissociating HO–H bonds. Then the unique structure was fabricated through in-situ photo-oxidation of Ni<sub>2</sub>P to Ni(OH)<sub>2</sub> on semiconductor like C<sub>3</sub>N<sub>4</sub> and subsequent selective photo-deposition of Pt on Ni(OH)<sub>2</sub> surface. Pt/Ni(OH)<sub>2</sub>–C<sub>3</sub>N<sub>4</sub> is much more active in photocatalytic HER, OER and overall water splitting compared with Pt, Ni(OH)<sub>2</sub> and spatially separated co-loaded Ni(OH)<sub>2</sub>–Pt on C<sub>3</sub>N<sub>4</sub>. And Pt/Ni(OH)<sub>2</sub>–C<sub>3</sub>N<sub>4</sub> achieves an AQE of 1.8% at 420 nm in overall water splitting by using only 0.3 wt% Pt, superior to most solid-state photocatalytic systems to date. Moreover, Pt/Ni(OH)<sub>2</sub> composite enables TiO<sub>2</sub> to split pure water in good stoichiometry. This work emphasizes the importance of H<sub>2</sub>O activation and may pave the way for enabling single semiconductors to efficiently split pure water.

### 1. Introduction

Solar-light-driven overall water splitting from semiconductor-based photocatalysis is a promising approach to solve the problem of energy shortage and environmental pollution caused by the excessive use of fossil fuels. However, the development of photocatalytic system with satisfying efficiency remains a big challenge [1,2]. In general, solar conversion efficiency is determined by three key factors: light absorption, charge transfer and surface redox reactions [3]. Many efforts have been devoted to improving the light absorption and charge transfer efficiency by designing and modulating the structure of semiconductors [4,5]. Meanwhile, cocatalysts are crucial to accelerate the surface redox kinetics, as well as enhance the charge transfer and photostability [6]. Generally, reduction and oxidation cocatalysts can promote either H<sub>2</sub> or O<sub>2</sub> evolution reactions (HER or OER), respectively [3]. Among them, Pt is considered as the best cocatalyst for H<sub>2</sub> generation attributed to its large work function and medium adsorption for proton [7], and (hydro) oxides of Co, Mn and Ni are widely used to accelerate O<sub>2</sub> generation [3,8–12]. Despite the progress in the utilization of these cocatalysts on improving the water splitting half-reactions with sacrificing agents,

pure water splitting remains an arduous task. The loading of both HER and OER cocatalysts on semiconductors, called as dual-cocatalyst strategy, has been used to achieve stoichiometric overall water splitting [13–17]. For example, CoP–Pt/C<sub>3</sub>N<sub>4</sub> was reported for water splitting, in which CoP serves as OER cocatalyst and Pt as HER cocatalyst, respectively [15]. However, reduction cocatalysts like Pt usually have poor ability in adsorbing H<sub>2</sub>O and cleaving H–OH bonds while oxidation cocatalysts like metal (hydro)oxides can't efficiently convert H<sup>\*</sup> to H<sub>2</sub> [18]. As these two kinds of cocatalysts are usually separate in the dual-cocatalyst systems, the acceleration of H<sub>2</sub>O activation and H<sup>\*</sup> recombination is hard to be realized simultaneously. Note that the activation of H<sub>2</sub>O molecules and dissociation of H–OH bonds are often determining steps with highest energy barrier, efficiently activating H<sub>2</sub>O is crucial to improve the photocatalytic efficiency [19]. Therefore, a robust cocatalyst–semiconductor system capable of both activating H<sub>2</sub>O and accelerating HER/OER kinetics without sacrificing agents is most desired.

Compared with the limited work on photocatalytic cocatalysts, electrochemical water splitting (co)catalysts have been widely studied [20–24]. Essentially, surface reactions including H–OH bond cleavage,

\* Corresponding author at: Key Laboratory for Green Chemical Technology of the Ministry of Education, School of Chemical Engineering and Technology, Tianjin University, Tianjin, 300072, China.

E-mail address: [jj\\_zou@tju.edu.cn](mailto:jj_zou@tju.edu.cn) (J.-J. Zou).

H–H and O–O bond formation are similar for both photo- and electrocatalysis despite the source of redox pairs is different, so the (co)catalysts used for electrocatalysis may also work well in photocatalysis [3,25,26]. It has been reported that combining metal hydroxides ( $\text{Ni(OH)}_2$  or  $\text{Co(OH)}_2$ ) with Pt can significantly improve the electrocatalytic HER activities [18,27–30]. In these systems, hydroxide provides active sites for  $\text{H}_2\text{O}$  dissociation while Pt promotes the recombination of  $\text{H}^*$  [19,27–30]. Also, metal hydroxides are efficient catalysts for OER [31–33].

Based on the above considerations, we speculated that the integration of Pt and  $\text{Ni(OH)}_2$  may be an ideal cocatalyst to well collaborate with semiconductor for photocatalytic water splitting, not only providing HER and OER sites but also synergistically activating  $\text{H}_2\text{O}$  molecules and cleaving H–OH bonds. Meanwhile, the most feasible and practical structure of the composite is Pt decorated  $\text{Ni(OH)}_2$  with low Pt content due to the high cost of noble metal. Herein, we report Pt cluster decorated  $\text{Ni(OH)}_2$  nanoparticles ( $\text{Pt}/\text{Ni(OH)}_2$ ) as robust cocatalysts anchored on semiconductors like  $\text{C}_3\text{N}_4$  for efficient photocatalytic overall water splitting, and provide a new and more efficient strategy for cocatalyst design in photocatalysis.

## 2. Experimental section

### 2.1. Computation

$\text{Pt}_4$  cluster loaded  $\beta\text{-Ni(OH)}_2$  (100) ( $\text{Pt}_4/\beta\text{-Ni(OH)}_2$  (100)) surface model was constructed to explore the synergistic role of  $\text{Ni(OH)}_2$  and Pt in water splitting.  $\beta\text{-Ni(OH)}_2$  (100) and Pt (111) slab models were constructed for comparison.  $\beta\text{-Ni(OH)}_2$  (100) surface was modeled by using a  $p(3 \times 2)$  unit cell with six layers, and the vacuum slab was 15 Å. The optimized cell parameters were  $a = b = 3.103 \text{ \AA}$ ,  $c = 4.492 \text{ \AA}$ . For  $\text{Pt}_4/\beta\text{-Ni(OH)}_2$  (100),  $\text{Pt}_4$  clusters with different structures were first optimized and the most stable cluster was selected and adsorbed on  $\beta\text{-Ni(OH)}_2$  (100) surface, the bottom three layers were fixed in their positions and others were relaxed during calculations. For Pt (111), a  $p(3 \times 3)$  unit cell with four layers periodically repeated slab model was constructed, the top two layers with adsorbates were fully relaxed during optimization. The density functional theory with the Hubbard model (DFT + U) calculations were performed by Vienna ab initio simulation package (VASP), and the projector augmented wave (PAW) method with Perdew-Burker-Ernzerhof (PBE) functional was implemented to deal with the nonlocal exchange correlation energy. The U value was set to 5.3 eV to eliminate the Ni 3d-states self-interaction error. The kinetic cutoff energy of 400 eV with the Brillouin zone integration of  $3 \times 3 \times 1$  k-point mesh was adopted during calculation process. The convergence critical of the force and energy of all atoms were set to  $0.05 \text{ eV \AA}^{-1}$  and  $1 \times 10^{-5} \text{ eV}$ , respectively. A  $6 \times 6 \times 6$  Monkhorst Pack k-point setup was used for cell optimization and all electron structure calculations. The adsorption energy ( $E_{\text{ads}}$ ) is defined according to the following formula:

$$E_{\text{ads}} = E_{\text{adsorbate/substrate}} - E_{\text{adsorbate}} - E_{\text{substrate}}$$

where  $E_{\text{adsorbate/substrate}}$ ,  $E_{\text{adsorbate}}$  and  $E_{\text{substrate}}$  represent the energies of the substrate with adsorbate species, the adsorbate molecules and the substrate, respectively [28,34].

### 2.2. Catalyst synthesis

$\text{C}_3\text{N}_4$  was prepared by thermal polycondensation of melamine at 550 °C for 4 h in muffle furnace.  $\text{Ni}_2\text{P}$  was synthesized using  $\text{NaH}_2\text{PO}_2$  as P source (see details in Supplementary Material). To get  $\text{Ni(OH)}_2/\text{C}_3\text{N}_4$ , calculated amount of  $\text{Ni}_2\text{P}$  and  $\text{C}_3\text{N}_4$  (20 mg) was dispersed in aqueous solution (100 mL) and irradiated under 300 W Xe-lamp for 2 h. The sample was collected, washed with ethanol and water and dried in a vacuum oven at 60 °C overnight. Then  $\text{Pt}/\text{Ni(OH)}_2\text{-C}_3\text{N}_4$  was prepared in-situ selective photo-reduction of  $\text{PtCl}_6^{2-}$  in a closed Pyrex top-

irradiation vessel. Typically,  $\text{Ni(OH)}_2/\text{C}_3\text{N}_4$  (20 mg) was dispersed in  $\text{H}_2\text{PtCl}_6$  aqueous solution (100 mL) and stirred for 20 min. The system was purged with Argon for 30 min to completely remove air and then irradiated for 2 h under 300 W Xe-lamp. Finally, the sample was collected, washed with ethanol and water and dried in a vacuum oven at 60 °C overnight.

$\text{Pt/C}_3\text{N}_4$  was prepared by above-mentioned in-situ photo-deposition of Pt on  $\text{C}_3\text{N}_4$ .  $\text{Ni(OH)}_2\text{-Pt/C}_3\text{N}_4$  was prepared via a process similar to that of  $\text{Ni(OH)}_2/\text{C}_3\text{N}_4$  while  $\text{Pt/C}_3\text{N}_4$  was used instead of  $\text{C}_3\text{N}_4$ . For  $\text{TiO}_2$ -based catalysts, Ti-deficient anatase was synthesized according to our previous work [35], and Degussa P25 was used as received. The fabrication of  $\text{Pt}/\text{Ni(OH)}_2\text{-anatase}$ ,  $\text{Pt}/\text{Ni(OH)}_2\text{-P25}$ ,  $\text{Ni(OH)}_2\text{-Pt/anatase}$  and  $\text{Ni(OH)}_2\text{-Pt/P25}$  is identical to that of  $\text{C}_3\text{N}_4$ -based counterparts while anatase (or P25) was used instead of  $\text{C}_3\text{N}_4$ .

### 2.3. Characterizations

X-ray diffraction (XRD) patterns were recorded using Bruker AXS D8 advanced diffractometer equipped with Cu K $\alpha$  radiation at a scanning rate of 5°/min. Scanning electron microscopy (SEM) images were observed using Hitachi S-4800 field emission scanning electron microscope. Transmission electron microscopy (TEM) analysis was carried out using Titan ETEM Themis aberration-corrected transmission electron microscope with an image Cs corrector and Tecnai G2 F-20 transmission electron microscope with a field-emission gun. Fourier transform infrared spectroscopy (FTIR) were obtained on a Bruker Vertex-70 Fourier transform infrared spectrometer. Raman spectra were obtained on a Renishaw inVia reflex Raman spectrometer. X-ray photoelectron spectroscopy (XPS) analysis was conducted with a PHI-1600 X-ray photoelectron spectrometer equipped with Al K $\alpha$  radiation and the binding energy was calibrated by the C 1 s peak (284.8 eV). Steady state photoluminescence (PL) spectra were measured by a Shimadzu UV-2600 spectrophotometer with an excitation light at 375 nm. UV-vis diffuse reflectance spectra were obtained from a Hitachi F-4600 fluorescence spectrophotometer equipped with a 60 mm diameter integrating sphere using  $\text{BaSO}_4$  as reference. Zeta potential was measured by Malvern Nano ZS Zetasizer.

Photoelectric properties were measured on a CHI 660B electrochemical system (Shanghai, China) using a standard three-electrode cell with a working electrode, a Pt wire counter electrode and an Ag/AgCl reference electrode.  $\text{Na}_2\text{SO}_4$  (1 mol/L) was used as the electrolyte solution. The working electrode was prepared by dip-coating catalyst slurry on F-doped tin oxide (FTO) glass electrode ( $1 \times 1.5 \text{ cm}^2$ ). All the investigated working electrodes were of similar thickness. Electrochemical impedance spectroscopy (EIS) measurements were carried out with a sinusoidal ac perturbation of 10 mV over the frequency of 0.1–10<sup>5</sup> Hz.

### 2.4. Photocatalytic test

Photocatalytic overall water splitting reaction was carried out in a closed Pyrex top-irradiation vessel (280 mL). 10 mg catalyst was dispersed in  $\text{H}_2\text{O}$  (100 mL) without any sacrificial agent. The reaction solution was purged with Argon for 30 min to completely remove air prior to irradiation. The reaction was conducted under a 300 W Xe-lamp (working current 15 A) and the temperature was maintained at 0 °C. The product was analyzed by gas chromatography equipped with a thermal conductive detector, using Argon as carrier gas. Photocatalytic  $\text{H}_2$  evolution was carried out using the same experimental setup as overall water splitting but with 10 vol% triethanolamine (TEOA) as sacrificial agent. And photocatalytic  $\text{O}_2$  evolution was carried out using the same experimental setup but with  $\text{AgNO}_3$  (0.01 mol/L) as sacrificial agent.

Apparent quantum efficiency (AQE) was measured using the same experimental setup under monochromatic light for 3 h. The wavelength of incident light was controlled by applying certain band-pass filters of

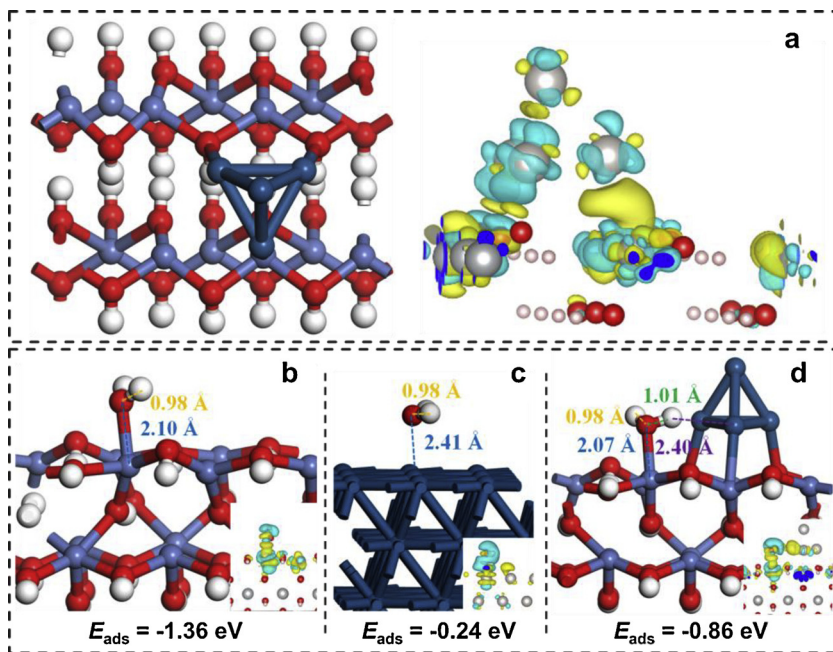


**Fig. 1.** Optimized structures and charge difference isosurfaces of (a)  $\text{Pt}_4/\beta\text{-Ni(OH)}_2$  (100),  $\text{H}_2\text{O}$  adsorbed on (b)  $\beta\text{-Ni(OH)}_2$  (100), (c) Pt (111) and (d)  $\text{Pt}_4/\beta\text{-Ni(OH)}_2$  (100). The dark blue, dusty blue, red and white balls represent Pt, Ni, O and H, respectively. Cyan and light yellow represent regions of hole and electron accumulations with isosurfaces value of  $0.005 \text{ e}\text{\AA}^{-3}$ . (For interpretation of the references to color in this figure legend, the reader is referred to the web version of this article).

full width at half maximum (FWHM) = 15 nm and the irradiation area was controlled as  $16 \text{ cm}^2$ . Light intensity was measured by a UV-A radiometer (Photoelectric Instrument Factory, Beijing Normal University). AQE was calculated as follow:

$$\text{AQE} = \frac{N_e}{N_p} \times 100\% = \frac{2 \times \text{number of evolved H}_2 \text{ molecules}}{\text{number of incident photons}} \times 100$$

where,  $N_e$  is the amount of reaction electrons,  $N_p$  is the amount of incident photons.

### 3. Results and discussion

#### 3.1. DFT calculation on the synergy of Pt and $\text{Ni(OH)}_2$ in water activation

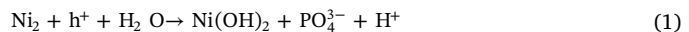
To confirm the superiority of  $\text{Pt}/\text{Ni(OH)}_2$  in water splitting process, DFT computation was first adopted by considering models of  $\text{Pt}_4/\beta\text{-Ni(OH)}_2$  (100),  $\beta\text{-Ni(OH)}_2$  (100) and Pt (111) (Fig. S1). Charge difference isosurfaces of  $\text{Pt}_4/\beta\text{-Ni(OH)}_2$  (Fig. 1a and S2) show that electrons of Pt transfer to  $\text{Ni(OH)}_2$  with an isovalue of  $+0.189 \text{ e/Bohr}$  for  $\text{Pt}_4$  cluster, exhibiting a strong interaction between Pt and  $\text{Ni(OH)}_2$ . Next the  $\text{H}_2\text{O}$  activation processes on these models were calculated. Fig. 1b and c show that  $\text{H}_2\text{O}$  is strongly chemisorbed on  $\beta\text{-Ni(OH)}_2$  (100) but weakly adsorbed on Pt (111) surface, both with O–H bonds almost unchanged. Basically, too strong or too weak adsorption will impede the subsequent  $\text{H}_2\text{O}$  dissociation as the O–H bond is not elongated enough. Notably, Fig. 1d shows moderate adsorption of  $\text{H}_2\text{O}$  over  $\text{Pt}_4/\beta\text{-Ni(OH)}_2$  surface with an adsorption energy of  $-0.86 \text{ eV}$ . Importantly,  $\text{H}_2\text{O}$  molecule is significantly distorted with one O–H bond increased to  $1.01 \text{ \AA}$  from original  $0.98 \text{ \AA}$ . The H atom of activated O–H bond points to  $\text{Pt}_4$  cluster whereas the O atom is adsorbed on Ni site. Hence, the cooperation of Pt and  $\text{Ni(OH)}_2$  can effectively activate  $\text{H}_2\text{O}$ , facilitating the cleavage of  $\text{HO-H}$  to  $\text{HO}^*$  and  $\text{H}^*$ , which is the critical step in water splitting [36].

#### 3.2. Strategy for in-situ fabricating $\text{Pt}/\text{Ni(OH)}_2$ on $\text{C}_3\text{N}_4$

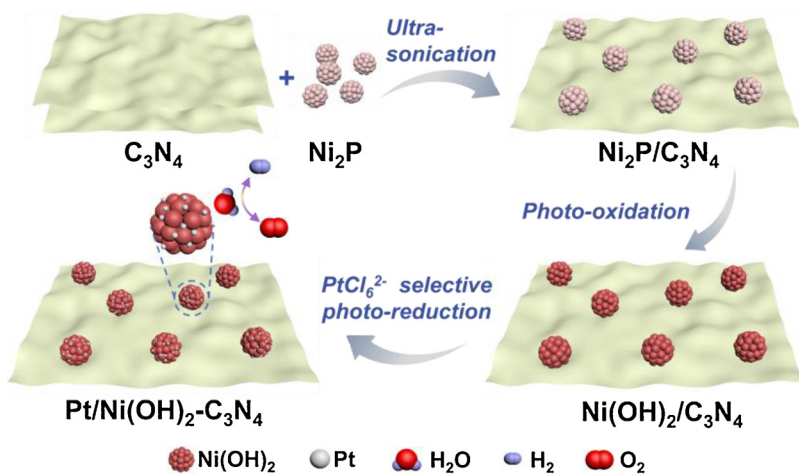
DFT calculations manifest the potential of  $\text{Pt}/\text{Ni(OH)}_2$  as cocatalyst for water splitting. However, to realize the synergy of Pt and  $\text{Ni(OH)}_2$  in photocatalysis, several issues must be considered. First, a good semiconductor is necessary to produce charge carriers, here we chose graphitic carbon nitride ( $\text{C}_3\text{N}_4$ ), a metal free semiconductor with controllable morphologies and optical properties [37–42]. Second, the

cocatalyst must be in nanosized and closely loaded on semiconductors for facile charge transfer, so we developed an in-situ deposition method to grow the cocatalyst on  $\text{C}_3\text{N}_4$ . Third, an intimate contact between  $\text{Ni(OH)}_2$  and Pt is vital for synergistic  $\text{H}_2\text{O}$  activation, necessitating the selective deposition of Pt on  $\text{Ni(OH)}_2$  rather than  $\text{C}_3\text{N}_4$ , which was realized through electrostatic interaction. With these considerations, we developed a unique photo-deposition method to fabricate Pt clusters decorated  $\text{Ni(OH)}_2$  nanoparticles on semiconductor like  $\text{C}_3\text{N}_4$  through photoinduced oxidation of  $\text{Ni}_2\text{P}$  to  $\text{Ni(OH)}_2$  and then selective deposition of Pt on  $\text{Ni(OH)}_2$  (Scheme 1).

Metal phosphides are easily oxidized to hydroxides at positive potential in the case of electrochemical OER [20–24,43]. Here we considered to in-situ grow  $\text{Ni(OH)}_2$  nanoparticles on  $\text{C}_3\text{N}_4$  via photo-oxidation of  $\text{Ni}_2\text{P}$  since the photoinduced holes of  $\text{C}_3\text{N}_4$  also have very positive oxidizing potential. In short,  $\text{Ni}_2\text{P}$  nanoparticles (Fig. S3) and  $\text{C}_3\text{N}_4$  were mixed (named as  $\text{Ni}_2\text{P}/\text{C}_3\text{N}_4$ ) in water and then irradiated. After that, the powders changed from gray to light yellow (Fig. S4). XRD pattern of the obtained powders (named as  $\text{Ni(OH)}_2/\text{C}_3\text{N}_4$ , the amount of  $\text{Ni(OH)}_2$  is 4.4 wt% if not specified) in Fig. 2a shows typical characteristic peaks of  $\text{C}_3\text{N}_4$  at  $13.0^\circ$  (100),  $27.4^\circ$  (002) (JCPDS 87-1526) and peaks of  $\beta\text{-Ni(OH)}_2$  at  $33.1^\circ$  (100),  $38.5^\circ$  (101),  $59.1^\circ$  (110) (JCPDS 14-0117) [13,28]. No peak of  $\text{Ni}_2\text{P}$  is detected even with its concentration as high as 10 wt% (Fig. S5a). FTIR, Raman and XPS analyses further confirm the absence of P species in  $\text{Ni(OH)}_2/\text{C}_3\text{N}_4$  (Fig. S5b-S5d). Moreover,  $\text{PO}_4^{3-}$  is detected in the supernatant after removing the solid (Fig. S6a) [44]. These results validate that  $\text{Ni}_2\text{P}$  has been oxidized to  $\text{Ni(OH)}_2$  deposited on  $\text{C}_3\text{N}_4$  and  $\text{PO}_4^{3-}$  dissolved in water. Notably,  $\text{C}_3\text{N}_4$  is necessary for the oxidation as pure  $\text{Ni}_2\text{P}$  is not changed after irradiation (Fig. S6b). Moreover, this process can also take place without  $\text{O}_2$  (Fig. S6c) and small amount of  $\text{H}_2$  is detected during the oxidation of  $\text{Ni}_2\text{P}$  (Fig. S6d). Therefore,  $\text{Ni}_2\text{P}$  is oxidized to  $\text{Ni(OH)}_2$  and  $\text{PO}_4^{3-}$  by photoinduced holes of  $\text{C}_3\text{N}_4$ , meanwhile the electrons reduce  $\text{H}_2\text{O}$  to  $\text{H}_2$ , as described in follows:



The second step to fabricate the photocatalyst is to selectively deposit Pt on the surface of  $\text{Ni(OH)}_2$  particles (named as  $\text{Pt}/\text{Ni(OH)}_2\text{-C}_3\text{N}_4$ , Pt is 0.3 wt% if not specified) by photoinduced reduction of  $\text{PtCl}_6^{2-}$ . The operation is similar to the photo-deposition of Pt in literature



**Scheme 1.** Schematic illustration of the photoinduced fabrication of  $\text{Pt}/\text{Ni}(\text{OH})_2\text{-C}_3\text{N}_4$ .

[38,45], but the structure is totally different since Pt is not randomly deposited on semiconductor. In this way  $\text{PtCl}_6^{2-}$  anions are preferably adsorbed on  $\text{Ni}(\text{OH})_2$  by electrostatic attraction and then in-situ reduced to small clusters by photoinduced electrons, because  $\text{C}_3\text{N}_4$  is negatively charged (with zeta potential of -12.1 mV in water) whereas  $\text{Ni}(\text{OH})_2$  shows strong positive surface charge (with zeta potential of 15.3 mV in water) from Zeta potential measurements. Hereon, as the potential of  $\text{Ni}^{2+}/\text{Ni} (\text{Ni}^{2+} + 2\text{e}^- = \text{Ni}, E^\circ = -0.23 \text{ V})$  is less negative than the conduction band of  $\text{C}_3\text{N}_4$  (about -1.0 V), the photoinduced electrons from  $\text{C}_3\text{N}_4$  can transfer towards  $\text{Ni}(\text{OH})_2$  domains to reduce the surface adsorbed  $\text{PtCl}_6^{2-}$  during photo-deposition [46]. There is no diffraction peak of Pt from XRD patterns due to its low content (Fig. 2a). Importantly, no single Pt particle is observed from TEM image,

although Energy dispersive X-ray (EDX) spectroscopy clearly reveals the existence of Pt (Fig. 2b). The high resolution TEM magnification of the small darker domains (red circle) in Fig. 2b shows no lattice fringes, indicating that they are just the stack of the edges of  $\text{C}_3\text{N}_4$  nanosheets rather than isolated Pt particles. Also, the high-angle-annular-dark-field scanning transmission electron microscopy (HAADF-STEM) image in Fig. 2d demonstrates that there is no isolated metal nanoparticle which will appear in the form of small bright dots. Besides, aberration corrected high resolution TEM (AC-HRTEM) image in Fig. 2c shows that Pt with particle size of sub-2.5 nm are selectively deposited on the surface of  $\text{Ni}(\text{OH})_2$ , and selected area electron diffraction (SAED) pattern of the particle shows diffraction rings of both  $\text{Ni}(\text{OH})_2$  and Pt. Electron energy loss spectroscopy (EELS) elemental mapping also shows that Pt is

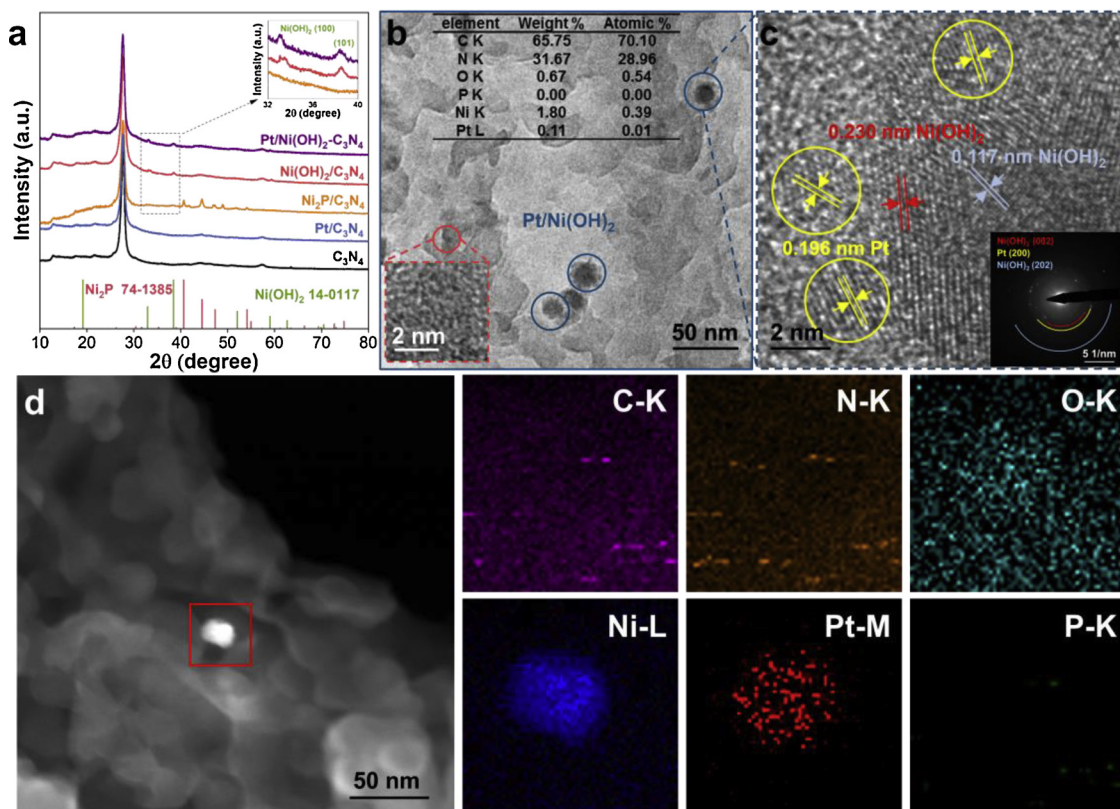


**Fig. 2.** (a) XRD patterns of fabricated samples. (b) TEM image with EDX element content, (c) AC-HRTEM image (magnification of the particle in b) with corresponding SAED pattern and (d) HAADF-STEM and EELS-mapping images of  $\text{Pt}/\text{Ni}(\text{OH})_2\text{-C}_3\text{N}_4$ . (For interpretation of the references to color in text, the reader is referred to the web version of this article.).

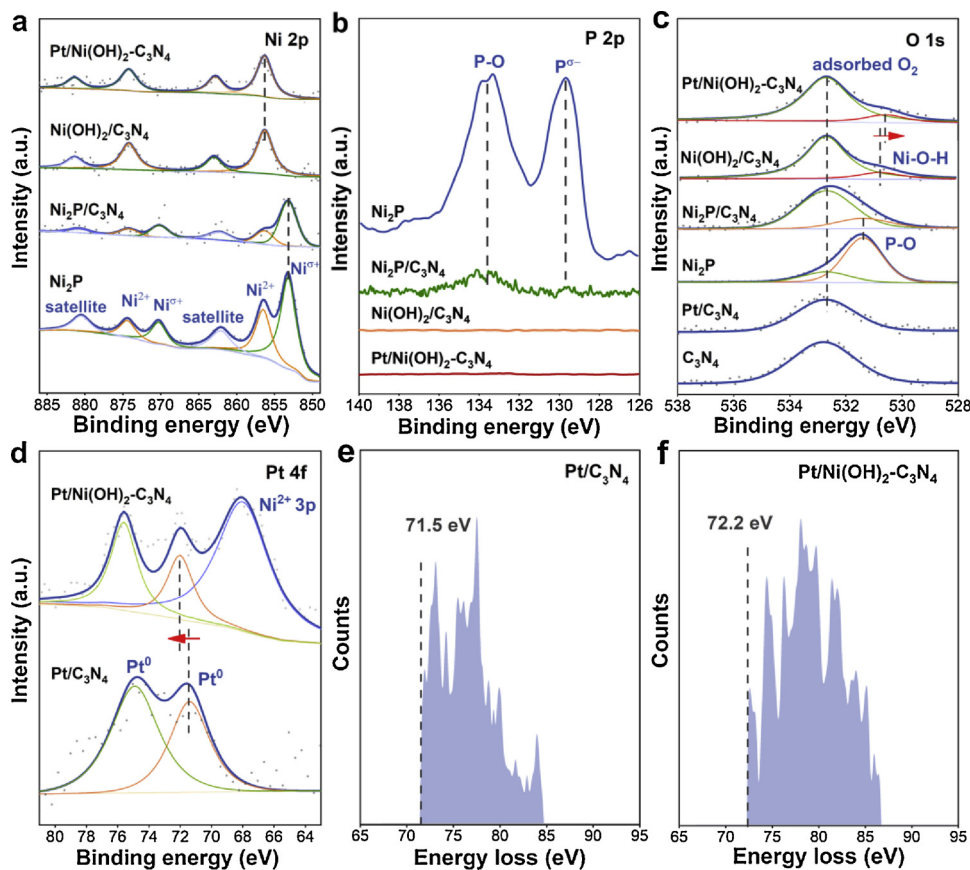


Fig. 3. (a) Ni 2p, (b) P 2p, (c) O 1s and (d) Pt 4f XPS spectra of fabricated samples. EELS edge spectra of Pt in (e) Pt/C<sub>3</sub>N<sub>4</sub> and (f) Pt/Ni(OH)<sub>2</sub>-C<sub>3</sub>N<sub>4</sub>.

dispersed only on the surface of Ni(OH)<sub>2</sub> (Fig. 2d). In contrast, with the same loading amount, Pt particles on Pt/C<sub>3</sub>N<sub>4</sub> is about 4–5 nm (Fig. S7) since PtCl<sub>6</sub><sup>2-</sup> ions are not easily adsorbed on C<sub>3</sub>N<sub>4</sub> due to electrostatic repulsion, and only a small amount of them are first reduced to form nuclei, which then act as electron reduction centers and grow into larger Pt particles.

As mentioned above, photoinduced holes can oxidize Ni<sub>2</sub>P to Ni(OH)<sub>2</sub> and electrons reduce PtCl<sub>6</sub><sup>2-</sup> to Pt. It is expected that these two redox reactions can take place at the same time. Thus we conducted a one-step synthesized Pt/Ni(OH)<sub>2</sub>-C<sub>3</sub>N<sub>4</sub> by irradiating the mixture of Ni<sub>2</sub>P, C<sub>3</sub>N<sub>4</sub> and PtCl<sub>6</sub><sup>2-</sup> in water and obtained the same structure (Fig. S8, see experimental details in Supplementary Material). There to simplify the synthesis, the catalyst fabricated by the one-step photodeposition method was used in the following work.

### 3.3. Electronic structure and optical property of Pt/Ni(OH)<sub>2</sub>-C<sub>3</sub>N<sub>4</sub>

Further chemical environment and interaction of Ni(OH)<sub>2</sub> and Pt were analyzed with XPS analysis. The Ni 2p<sub>3/2</sub> edge of Ni<sub>2</sub>P (Fig. 3a) can be deconvoluted into three peaks at 852.9, 856.3 and 862.3 eV, related to Ni<sup>0+</sup> ( $0 < \sigma < 2$ ) of Ni<sub>2</sub>P, Ni<sup>2+</sup> of Ni(OH)<sub>2</sub> formed by surface oxidation and their satellite peak, respectively [47,48]. For Ni(OH)<sub>2</sub>/C<sub>3</sub>N<sub>4</sub> and Pt/Ni(OH)<sub>2</sub>-C<sub>3</sub>N<sub>4</sub>, the peaks of Ni<sup>0+</sup> disappear and only the peaks of Ni<sup>2+</sup> are observed, and P signals disappear in P 2p spectra (Fig. 3b). Also in O 1s spectra (Fig. 3c), the peaks at 531.7 eV assigned to P–O bond disappear, while a new peak ascribed to Ni–O–H (at about 530.8 eV) is observed [28]. So it further confirms Ni<sub>2</sub>P is completely converted to Ni(OH)<sub>2</sub>, in line with the XRD and TEM results. Besides, Fig. S9–S10 indicate C<sub>3</sub>N<sub>4</sub> remains unchanged after loading cocatalyst. In Fig. 3d, the Pt 4f<sub>7/2</sub> peak of Pt/C<sub>3</sub>N<sub>4</sub> mainly locates at 71.4 eV and can be assigned to Pt<sup>0</sup> [13,49]. However, this peak is obviously blue-shifted for Pt/Ni(OH)<sub>2</sub>-C<sub>3</sub>N<sub>4</sub>, which is also revealed by

EELS spectra (Fig. 3e and f). On the contrary, the O 1s peak of Pt/Ni(OH)<sub>2</sub>-C<sub>3</sub>N<sub>4</sub> is red-shifted relative to Ni(OH)<sub>2</sub>/C<sub>3</sub>N<sub>4</sub>. This binding energy shift suggests a strong interaction between Pt and O, originating from the electron transfer from Pt to Ni(OH)<sub>2</sub> via the formation of some Pt<sup>0+</sup>-O<sup>0-</sup> bonds, in accord with DFT predication. The electron-deficient Pt<sup>0+</sup> may be more capable of trapping electrons, and it has been reported that Pt in higher oxidation state can act as efficient HER site as well as suppress H<sub>2</sub> back-oxidation, being a better cocatalyst than metallic Pt<sup>0</sup> [50].

Then UV-vis spectroscopy was performed to analyze the optical properties of the catalysts (Fig. S11a), which shows that the presence of Ni(OH)<sub>2</sub> or Pt does not obviously change the absorption edge. Although this structure is not as efficient as C<sub>3</sub>N<sub>4</sub> co-loaded with isolated Pt and Ni(OH)<sub>2</sub> in the aspect of charge separation (see details in section 3.5), PL spectra in Fig. S11b reveal that Pt/Ni(OH)<sub>2</sub>-C<sub>3</sub>N<sub>4</sub> is much more efficient than Pt/C<sub>3</sub>N<sub>4</sub> and Ni(OH)<sub>2</sub>/C<sub>3</sub>N<sub>4</sub>, probably because the Pt<sup>0+</sup>-O<sup>0-</sup> bonds can accelerate the redistribution of charge carriers [47,48,51]. EIS curve (Fig. S11c) shows a semi-circle with smallest radius for Pt/Ni(OH)<sub>2</sub>-C<sub>3</sub>N<sub>4</sub>, indicating its smallest charge transfer resistance. Pt/Ni(OH)<sub>2</sub>-C<sub>3</sub>N<sub>4</sub> also endows a highest photocurrent intensity (Fig. S11d). Therefore, it can be seen the synergistic cocatalyst is able to accelerate charge separation and transfer more effectively than individual cocatalysts in photocatalysis.

### 3.4. Photocatalytic HER and OER performance of Pt/Ni(OH)<sub>2</sub>-C<sub>3</sub>N<sub>4</sub>

The photocatalytic HER and OER performance of the fabricated samples were first measured with TEOA and AgNO<sub>3</sub> as sacrificing agents, respectively. As shown in Fig. 4a, Ni(OH)<sub>2</sub>/C<sub>3</sub>N<sub>4</sub> can catalyze both HER and OER although the activity is relatively low, and an optimal loading of 4.4 wt% Ni(OH)<sub>2</sub> shows the highest activity. Fig. S12 shows pure Ni(OH)<sub>2</sub> possesses negligible activity, indicating that it

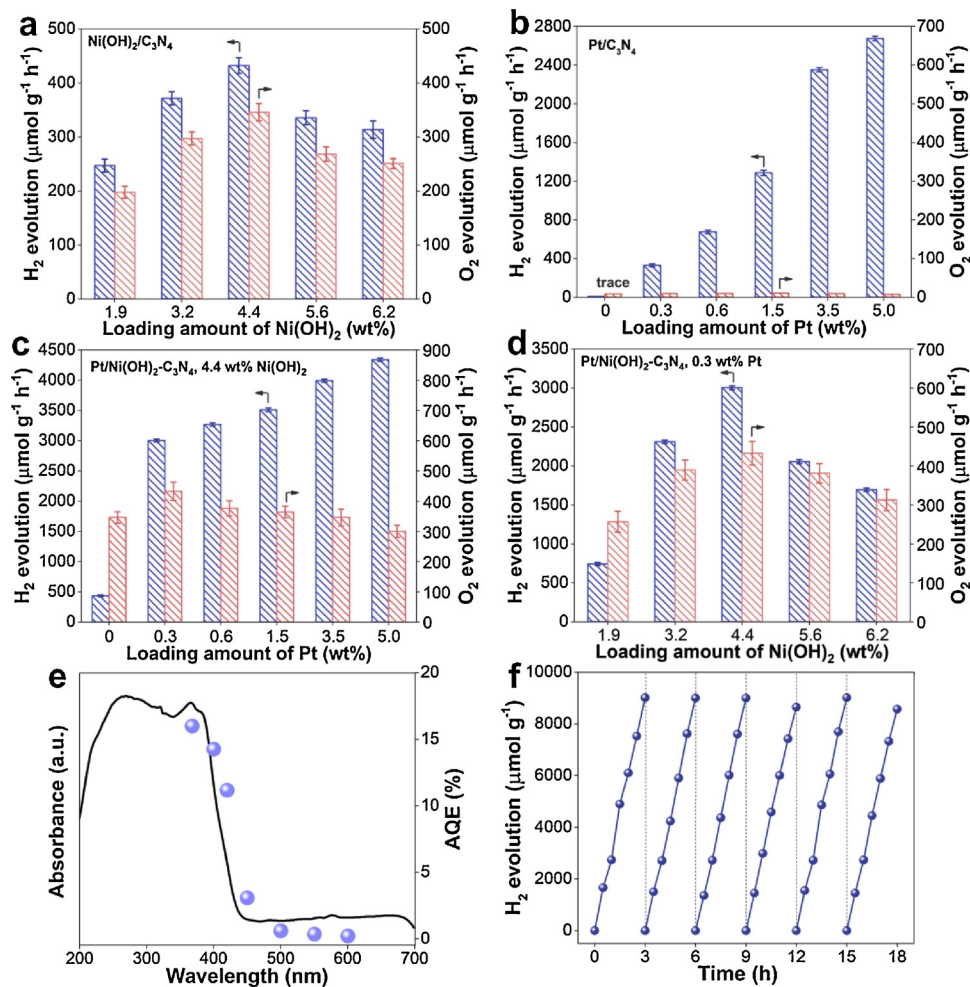


**Fig. 4.** (a–d) Photocatalytic HER and OER performance of fabricated samples with TEOA and AgNO<sub>3</sub> as sacrificing agents, respectively (average in 3 h). (e) Wavelength dependent AQE (blue dots) of photocatalytic HER and (f) long-term HER test by Pt/Ni(OH)<sub>2</sub>-C<sub>3</sub>N<sub>4</sub> with 0.3 wt% Pt and 4.4 wt% Ni(OH)<sub>2</sub>. (For interpretation of the references to color in this figure legend, the reader is referred to the web version of this article).

mainly functions as cocatalyst here. Pt/C<sub>3</sub>N<sub>4</sub> exhibits a higher HER activity than Ni(OH)<sub>2</sub>/C<sub>3</sub>N<sub>4</sub> with the same amount of cocatalyst but produces negligible O<sub>2</sub>, and the HER activity increases with the amount of Pt in the studied range (Fig. 4b). Importantly, Fig. 4c and d show that Pt/Ni(OH)<sub>2</sub>-C<sub>3</sub>N<sub>4</sub> exhibits much enhanced activity for both HER and OER compared with Ni(OH)<sub>2</sub>/C<sub>3</sub>N<sub>4</sub> and Pt/C<sub>3</sub>N<sub>4</sub>. The HER rate of Pt/Ni(OH)<sub>2</sub>-C<sub>3</sub>N<sub>4</sub> increases with the amount of Pt, but does not change much when the Pt content exceeds 0.3 wt%. The OER rate also reaches highest with 0.3 wt% Pt. Nevertheless, Pt/Ni(OH)<sub>2</sub>-C<sub>3</sub>N<sub>4</sub> with 4.4 wt% Ni(OH)<sub>2</sub> shows the highest photocatalytic activity in both HER and OER.

Especially, for HER, the activity of Pt/Ni(OH)<sub>2</sub>-C<sub>3</sub>N<sub>4</sub> is much higher than that of Pt/C<sub>3</sub>N<sub>4</sub> within the whole experimental range (Fig. 4b and c). Specifically, with 4.4 wt% Ni(OH)<sub>2</sub> and 0.3 wt% Pt, the activity of Pt/Ni(OH)<sub>2</sub>-C<sub>3</sub>N<sub>4</sub> reaches 3005 μmol g<sup>-1</sup> h<sup>-1</sup>, which is 9.1 times of Pt/C<sub>3</sub>N<sub>4</sub> and 8.2 times of Ni(OH)<sub>2</sub>/C<sub>3</sub>N<sub>4</sub> with the same amount of corresponding cocatalyst. The activity is also obvious higher than 5 wt% Pt/C<sub>3</sub>N<sub>4</sub> (2675 μmol g<sup>-1</sup> h<sup>-1</sup>), being promising to reduce the cost of photocatalyst. Also, Pt/Ni(OH)<sub>2</sub>-C<sub>3</sub>N<sub>4</sub> achieves an AQE of 11.2% at 420 nm with only 0.3 wt% Pt (Fig. 4e), better than most reported C<sub>3</sub>N<sub>4</sub>-based catalysts with higher Pt content of 3 wt% (Table S1), note that the C<sub>3</sub>N<sub>4</sub> used here is synthesized by directly thermal polycondensation of melamine. Long-term test (Fig. 4f) shows no noticeable decrease in activity within 18 h, indicating the robust stability of Pt/Ni(OH)<sub>2</sub>-C<sub>3</sub>N<sub>4</sub>.

### 3.5. Photocatalytic overall water splitting using Pt/Ni(OH)<sub>2</sub> as cocatalyst

More importantly, Pt/Ni(OH)<sub>2</sub>-C<sub>3</sub>N<sub>4</sub> exhibits excellent performance in overall water splitting without any sacrificing or pH adjusting agents. With 4.4 wt% Ni(OH)<sub>2</sub> and 0.3 wt% Pt, it achieves a HER rate of 425.7 μmol g<sup>-1</sup> h<sup>-1</sup> and stoichiometric OER rate of 201.2 μmol g<sup>-1</sup> h<sup>-1</sup> (Fig. 5a) in pure water. The AQE at 420 nm reaches 1.8% (Fig. 5b), exceeding most solid-state overall water splitting photocatalysts in pure water (Table S2). Long-term test also reveals a robust stability for pure water splitting (Fig. 5c). In addition, an optimal ratio of Pt (0.3 wt%) and Ni(OH)<sub>2</sub> (4.4 wt%) is essential to achieve efficient stoichiometric water splitting. Fig. 5a shows that no O<sub>2</sub> is generated without Ni(OH)<sub>2</sub> and no H<sub>2</sub> without Pt in pure water, indicating these two materials function as OER and HER sites, respectively. The amount of Pt and Ni(OH)<sub>2</sub> will lead to different amount of available reduction and oxidation sites, respectively. The number of reduction sites can affect the H<sub>2</sub> evolution rate while the number of oxidation sites affects O<sub>2</sub> evolution kinetics, which result in the varied ratio of produced H<sub>2</sub>/O<sub>2</sub> [4,14]. And the H<sub>2</sub>/O<sub>2</sub> ratio is higher than 2:1 at Pt amount > 0.3 wt% (case of excessive reduction sites), whereas lower than 2:1 at Ni(OH)<sub>2</sub> amount > 4.4 wt% (case of excessive oxidation sites), even they produce more H<sub>2</sub> and O<sub>2</sub>. In these cases, the excessive holes or electrons will finally deactivate the catalyst. Taking Pt/C<sub>3</sub>N<sub>4</sub> as examples, only small amount of H<sub>2</sub> was observed during reaction and the activity dropped rapidly, indicating that such systems are not sustainable for water splitting (Fig. S13). In this condition, the photocatalyst will act as

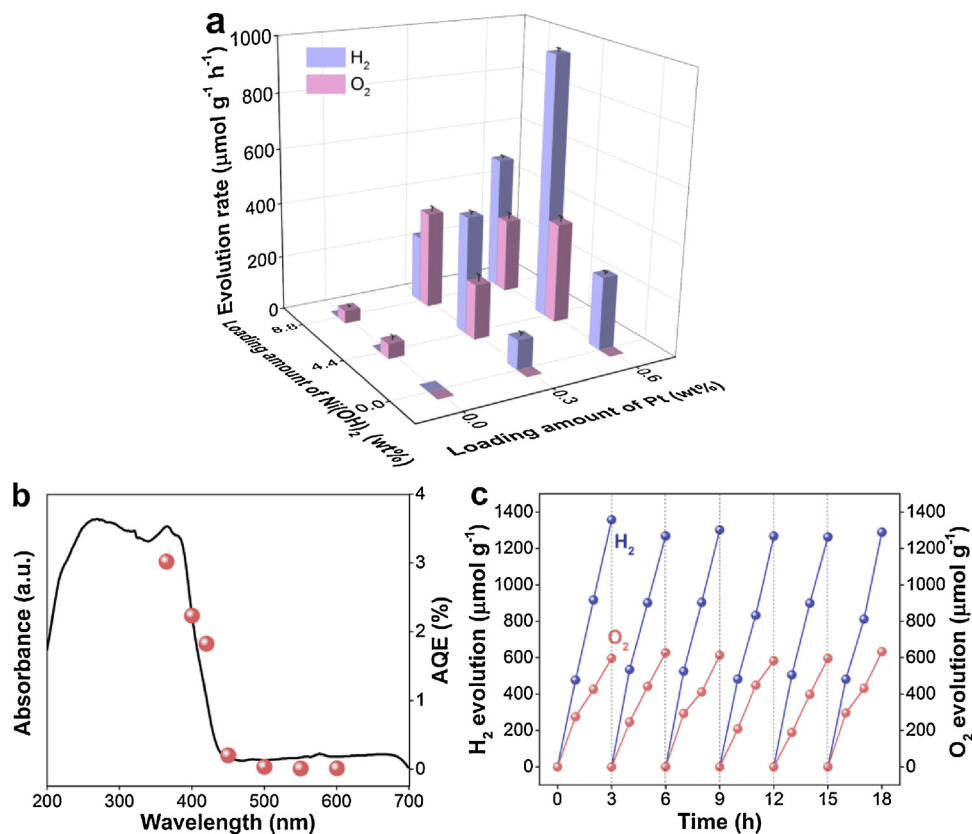


**Fig. 5.** (a) Averaged photocatalytic overall water splitting rate by  $\text{Pt}/\text{Ni(OH)}_2\text{-C}_3\text{N}_4$  with different cocatalysts content in 3 h. (b) Wavelength dependent AQE (pink dots) and (c) long-term test of  $\text{Pt}/\text{Ni(OH)}_2\text{-C}_3\text{N}_4$  with 0.3 wt% Pt and 4.4 wt%  $\text{Ni(OH)}_2$  in pure water.

sacrificing agents to consume the excessive holes and lead to its partial decomposition [4,14].

Controlled experiments were further conducted to verify the superiority of the synergistic  $\text{Pt}/\text{Ni(OH)}_2$  cocatalyst (Fig. 6a). Pt deposited  $\text{Ni(OH)}_2$  synthesized by chemical reduction of  $\text{PtCl}_6^{2-}$  on  $\text{Ni(OH)}_2$  nanosheet (named as crPt/ $\text{Ni(OH)}_2$ , Fig. S14a) shows negligible activity since both  $\text{Ni(OH)}_2$  and Pt have poor ability in absorbing light to generate charge carriers. The mixture of aforesaid crPt/ $\text{Ni(OH)}_2$  and  $\text{C}_3\text{N}_4$  (crPt/ $\text{Ni(OH)}_2\text{-C}_3\text{N}_4$ ) shows an enhanced HER rate, demonstrating the composite of  $\text{Pt}/\text{Ni(OH)}_2$  as very active cocatalyst. For  $\text{Ni(OH)}_2\text{-Pt/C}_3\text{N}_4$ , about 20 nm- $\text{Ni(OH)}_2$  particles and fine Pt nanoparticles are spatially separated on  $\text{C}_3\text{N}_4$  (Fig. S14b), which is similar to the reported dual-catalyst modified photocatalyst [15]. Although  $\text{Ni(OH)}_2\text{-Pt/C}_3\text{N}_4$  exhibits an enhanced charge separation property than  $\text{Pt}/\text{Ni(OH)}_2\text{-C}_3\text{N}_4$  (Fig. S15), its HER activity is only half of the latter. In pure water,  $\text{Ni(OH)}_2\text{-Pt/C}_3\text{N}_4$  also exhibits a stoichiometric water splitting

activity with HER rate of  $175.2 \mu\text{mol g}^{-1} \text{h}^{-1}$  and  $\text{O}_2$  evolution rate of  $85.3 \mu\text{mol g}^{-1} \text{h}^{-1}$  (Fig. 6a). However, its activity is only 50% of  $\text{Pt}/\text{Ni(OH)}_2\text{-C}_3\text{N}_4$ , which highlights the advantage of  $\text{Pt}/\text{Ni(OH)}_2$  composited cocatalyst compared with the common dual-cocatalyst. Notably, the fabrication of  $\text{Ni(OH)}_2\text{-Pt/C}_3\text{N}_4$  including the transformation of  $\text{Ni}_2\text{P}$  precursor to  $\text{Ni(OH)}_2$  and photo-deposition of Pt on  $\text{C}_3\text{N}_4$  is similar to  $\text{Pt}/\text{Ni(OH)}_2\text{-C}_3\text{N}_4$  despite the different preparation sequence, thus the two kinds of catalysts possess the same cocatalyst content, similar catalyst morphologies and exposed active areas (Fig. 2b and S14b). Therefore, the enhanced water splitting performance of  $\text{Pt}/\text{Ni(OH)}_2\text{-C}_3\text{N}_4$  is mainly attributed to the strong synergy of Pt and  $\text{Ni(OH)}_2$  with intimate contact in  $\text{H}_2\text{O}$  activation.

The  $\text{Pt}/\text{Ni(OH)}_2$  cocatalyst is also extended to other semiconductors like  $\text{TiO}_2$ . Note that stoichiometric water splitting is seldom achieved using single  $\text{TiO}_2$  semiconductor although its band level is suitable for both HER and OER [52,53]. The Zeta potential of anatase and P25 are

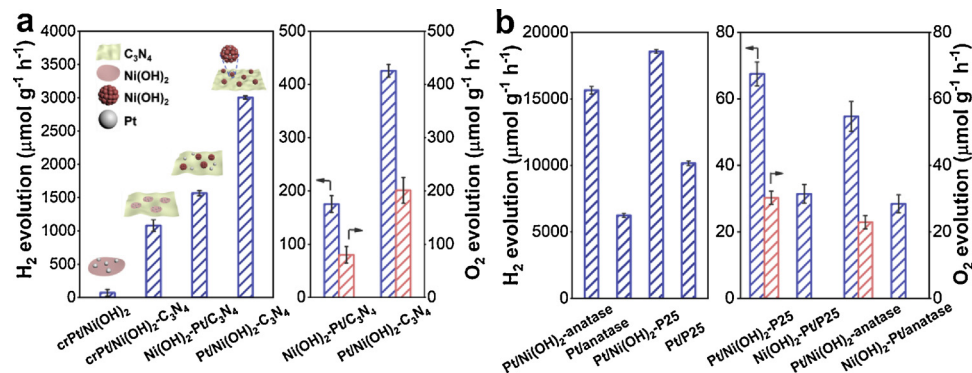


**Fig. 6.** Averaged photocatalytic HER (left) and overall water splitting (right) rate in 3 h of different cocatalysts loaded (a)  $\text{C}_3\text{N}_4$  and (b)  $\text{TiO}_2$ . Pt content is 6.8 wt% for crPt/ $\text{Ni(OH)}_2$  (0.3/4.4 wt%). For other samples,  $\text{Ni(OH)}_2$  content is 4.4 wt% and Pt is 0.3 wt%.

-9.4 mV and -2.5 mV in water, respectively, ensuring the selectively deposition of Pt on  $\text{Ni(OH)}_2$ , like the case of  $\text{C}_3\text{N}_4$ . Fig. 6b shows that  $\text{Pt}/\text{Ni(OH)}_2\text{-P25}$  and  $\text{Pt}/\text{Ni(OH)}_2\text{-anatase}$  both achieve overall water splitting. For comparison, when  $\text{Ni(OH)}_2$  and Pt are separated on P25 ( $\text{Ni(OH)}_2\text{-Pt/P25}$ ) or anatase ( $\text{Ni(OH)}_2\text{-Pt/anatase}$ ), they cannot produce any oxygen in pure water. These results again emphasize the strong synergistic cocatalyst can boost  $\text{H}_2\text{O}$  splitting. In addition,  $\text{Pt}/\text{Ni(OH)}_2\text{-P25}$  and  $\text{Pt}/\text{Ni(OH)}_2\text{-anatase}$  also show higher HER activity than the counterparts only with Pt as cocatalyst.

#### 4. Conclusion

In summary, we reported a strongly synergistic composited cocatalyst to boost  $\text{H}_2\text{O}$  activation for photocatalytic overall water splitting through an in-situ photoinduced strategy. The intimate contact between nanosized Pt and  $\text{Ni(OH)}_2$  brings up a strong  $\text{Pt}^{0+}\text{-O}^{\sigma-}$  interaction, which enhances  $\text{H}_2\text{O}$  activation along with accelerates charge transfer. More importantly, this structure facilitates the adsorption of  $\text{H}_2\text{O}$ , making  $\text{H-OH}$  bonds greatly activated and easily cleaved. As a result,  $\text{Pt}/\text{Ni(OH)}_2\text{-C}_3\text{N}_4$  is much more effective for photocatalytic HER, OER and overall water splitting compared with Pt,  $\text{Ni(OH)}_2$  and spatially separated  $\text{Pt-Ni(OH)}_2$  loaded  $\text{C}_3\text{N}_4$ . Especially, using only 0.3 wt% Pt,  $\text{Pt}/\text{Ni(OH)}_2\text{-C}_3\text{N}_4$  achieves an AQE of 11.2% for HER with sacrificing agents, and an AQE of 1.8% for overall water splitting at 420 nm without any sacrificing agents. Also,  $\text{Pt}/\text{Ni(OH)}_2$  enables  $\text{TiO}_2$  to split water with considerable activity. Consequently, this work emphasizes the importance of  $\text{H}_2\text{O}$  activation and elucidates a promising method for designing highly efficient photocatalytic system to achieve overall water splitting.

#### Conflict of interests

The authors declare no conflict of interests.

#### Acknowledgements

The authors appreciate the support from the National Natural Science Foundation of China (51661145026, 21676193, 21506156) and the Tianjin Municipal Natural Science Foundation (16JCQNJC05200).

#### Appendix A. Supplementary data

Supplementary material related to this article can be found, in the online version, at doi:<https://doi.org/10.1016/j.apcatb.2018.10.051>.

#### References

- J. Low, J. Yu, M. Jaroniec, S. Wageh, A.A. Al-Ghamdi, Heterojunction photocatalysts, *Adv. Mater.* 29 (2017) 1601694.
- S. Liu, F. Chen, S. Li, X. Peng, Y. Xiong, Enhanced photocatalytic conversion of greenhouse gas  $\text{CO}_2$  into solar fuels over  $\text{g-C}_3\text{N}_4$  nanotubes with decorated transparent ZIF-8 nanoclusters, *Appl. Catal. B* 211 (2017) 1–10.
- S. Chen, T. Takata, K. Domen, Particulate photocatalysts for overall water splitting, *Nat. Rev. Mater.* 2 (2017) 17050.
- L. Lin, C. Wang, W. Ren, H. Qu, Y. Zhang, X. Wang, Photocatalytic overall water splitting by conjugated semiconductors with crystalline poly (triazine imide) frameworks, *Chem. Sci.* 8 (2017) 5506–5511.
- N. Meng, J. Ren, Y. Liu, Y. Huang, T. Petit, B. Zhang, Engineering oxygen-containing and amino groups into two-dimensional atomically-thin porous polymeric carbon nitrogen for enhanced photocatalytic hydrogen production, *Energy Environ. Sci.* 11 (2018) 566–571.
- J. Yang, D. Wang, H. Han, C. Li, Roles of cocatalysts in photocatalysis and photoelectrocatalysis, *Acc. Chem. Res.* 46 (2013) 1900–1909.
- W. Sheng, M. Mzouyint, J.G. Chen, Y. Yan, Correlating the hydrogen evolution reaction activity in alkaline electrolytes with the hydrogen binding energy on monometallic surfaces, *Energy Environ. Sci.* 6 (2013) 1509–1512.
- H. Zhang, W. Tian, L. Zhou, H. Sun, M. Tade, S. Wang, Monodisperse  $\text{Co}_3\text{O}_4$  quantum dots on porous carbon nitride nanosheets for enhanced visible-light-driven water oxidation, *Appl. Catal. B* 223 (2018) 2–9.
- L. Zhang, C. Yang, Z. Xie, X. Wang, Cobalt manganese spinel as an effective cocatalyst for photocatalytic water oxidation, *Appl. Catal. B* 224 (2018) 886–894.
- T. Yoshihaga, M. Saruyama, A. Xiong, Y. Ham, Y. Kuang, R. Niishiro, S. Akiyama, M. Sakamoto, T. Hisatomi, K. Domen, T. Teranishi, Boosting photocatalytic overall water splitting by Co doping into  $\text{Mn}_3\text{O}_4$  nanoparticles as oxygen evolution cocatalysts, *Nanoscale* 10 (2018) 10420–10427.
- M. Tahir, L. Pan, F. Idrees, X. Zhang, L. Wang, J.-J. Zou, Z.L. Wang, Electrocatalytic oxygen evolution reaction for energy conversion and storage: A comprehensive review, *Nano Energy* 37 (2017) 136–157.
- X. Li, S. Liu, K. Fan, Z. Liu, B. Song, J. Yu, MOF-based transparent passivation layer modified  $\text{ZnO}$  nanorod arrays for enhanced photo-electrochemical water splitting, *Adv. Energy Mater.* 8 (2018) 1800101.
- G. Zhang, Z.-A. Lan, L. Lin, S. Lin, X. Wang, Overall water splitting by  $\text{Pt/g-C}_3\text{N}_4$  photocatalysts without using sacrificial agents, *Chem. Sci.* 7 (2016) 3062–3066.
- C.M. Wolff, P.D. Frischmann, M. Schulze, B.J. Bohn, R. Wein, P. Livadas, M.T. Carlson, F. Jäckel, J. Feldmann, F. Würthner, J.K. Stolarczyk, All-in-one visible-light-driven water splitting by combining nanoparticulate and molecular cocatalysts on  $\text{CdS}$  nanorods, *Nat. Energy* 3 (2018) 862–869.
- Z. Pan, Y. Zheng, F. Guo, P. Niu, X. Wang, Decorating  $\text{CoP}$  and Pt nanoparticles on graphitic carbon nitride nanosheets to promote overall water splitting by conjugated polymers, *ChemSusChem* 10 (2017) 87–90.
- Q. Wang, T. Hisatomi, Y. Suzuki, Z. Pan, J. Seo, M. Katayama, T. Minegishi, H. Nishiyama, T. Takata, K. Seki, A. Kudo, T. Yamada, K. Domen, Particulate photocatalyst sheets based on carbon conductor layer for efficient Z-scheme pure-water splitting at ambient pressure, *J. Am. Chem. Soc.* 139 (2017) 1675–1683.
- Q. Wang, T. Hisatomi, Q. Jia, H. Tokudome, M. Zhong, C. Wang, Z. Pan, T. Takata, M. Nakabayashi, N. Shibata, Y. Li, I.D. Sharp, A. Kudo, T. Yamada, K. Domen, Scalable water splitting on particulate photocatalyst sheets with a solar-to-hydrogen energy conversion efficiency exceeding 1%, *Nat. Mater.* 15 (2016) 611–615.
- R. Subbaraman, D. Tripkovic, D. Strmcnik, K.-C. Chang, M. Uchimura, A.P. Paulikas, V. Stamenkovic, N.M. Markovic, Enhancing hydrogen evolution activity in water splitting by tailoring  $\text{Li}^+\text{-Ni(OH)}_2\text{-Pt}$  interfaces, *Science* 334 (2011) 1256–1260.
- N. Mahmood, Y. Yao, J.-W. Zhang, L. Pan, X. Zhang, J.-J. Zou, Electrocatalysts for hydrogen evolution in alkaline electrolytes: mechanisms, challenges, and prospective solutions, *Adv. Sci.* 5 (2018) 1700464.
- W. Huang, X.-Y. Ma, H. Wang, R. Feng, J. Zhou, P.N. Duchesne, P. Zhang, F. Chen, N. Han, F. Zhao, J. Zhou, W.-B. Cai, Y. Li, Promoting effect of  $\text{Ni(OH)}_2$  on palladium nanocrystals leads to greatly improved operation durability for electrocatalytic ethanol oxidation in alkaline solution, *Adv. Mater.* 29 (2017) 1703057.
- C.-H. Kuo, I.M. Mosa, A.S. Poyraz, S. Biswas, A.M. El-Sawy, W. Song, Z. Luo, S.-Y. Chen, J.F. Rusling, J. He, S.L. Suib, Robust mesoporous manganese oxide catalysts for water oxidation, *ACS Catal.* 5 (2015) 1693–1699.
- Z. Zhou, N. Mahmood, Y. Zhang, L. Pan, L. Wang, X. Zhang, J.-J. Zou, CoP nanoparticles embedded in P and N co-doped carbon as efficient bifunctional electrocatalyst for water splitting, *J. Energy Chem.* 26 (2017) 1223–1230.
- C. Li, X. Han, F. Cheng, Y. Hu, C. Chen, J. Chen, Phase and composition controllable synthesis of cobalt manganese spinel nanoparticles towards efficient oxygen electrocatalysis, *Nat. Commun.* 6 (2015) 7345.
- J.S. Kim, B. Kim, H. Kim, K. Kang, Recent progress on multimetal oxide catalysts for the oxygen evolution reaction, *Adv. Energy Mater.* 8 (2018) 1702774.
- Z.-F. Huang, J. Song, K. Li, M. Tahir, Y.-T. Wang, L. Pan, L. Wang, X. Zhang, J.-J. Zou, Hollow cobalt-based bimetallic sulfide polyhedra for efficient all-pH-value electrochemical and photocatalytic hydrogen evolution, *J. Am. Chem. Soc.* 138 (2016) 1359–1365.
- J.-J. Zou, C.-J. Liu, Y.-P. Zhang, Control of the metal-support interface of  $\text{NiO}$ -loaded photocatalysts via cold plasma treatment, *Langmuir* 22 (2006) 2334–2339.
- Z. Xing, C. Han, D. Wang, Q. Li, X. Yang, Ultrafine Pt nanoparticle-decorated  $\text{Co(OH)}_2$  nanosheet arrays with enhanced catalytic activity toward hydrogen evolution, *ACS Catal.* 7 (2017) 7131–7135.
- X. Yu, J. Zhao, L. Zheng, Y. Tong, M. Zhang, G. Xu, C. Li, G. Shi, Hydrogen evolution reaction in alkaline media: alpha- or beta-nickel hydroxide on the surface of platinum? *ACS Energy Lett.* 3 (2018) 237–244.
- L. Wang, Y. Zhu, Z. Zeng, C. Lin, M. Giroux, L. Jiang, Y. Han, J. Greeley, C. Wang, J. Jin, Platinum-nickel hydroxide nanocomposites for electrocatalytic reduction of water, *Nano Energy* 31 (2017) 456–461.
- H. Yin, S. Zhao, K. Zhao, A. Mqsit, H. Tang, L. Chang, H. Zhao, Y. Gao, Z. Tang, Ultrathin platinum nanowires grown on single-layered nickel hydroxide with high hydrogen evolution activity, *Nat. Commun.* 6 (2015) 6430.
- C. Luan, G. Liu, Y. Liu, L. Yu, Y. Wang, Y. Xiao, H. Qiao, X. Dai, X. Zhang, Structure effects of 2D materials on  $\alpha$ -nickel hydroxide for oxygen evolution reaction, *ACS Nano* 12 (2018) 3875–3885.
- J. Zhang, J. Liu, L. Xi, Y. Yu, N. Chen, S. Sun, W. Wang, K.M. Lange, B. Zhang, Single-atom Au/NiFe layered double hydroxide electrocatalyst: probing the origin of activity for oxygen evolution reaction, *J. Am. Chem. Soc.* 140 (2018) 3876–3879.
- L. Yu, J.F. Yang, B.Y. Guan, Y. Lu, X.W. Lou, Hierarchical hollow nanoprisms based on ultrathin Ni-Fe layered double hydroxide nanosheets with enhanced electrocatalytic activity towards oxygen evolution, *Angew. Chem. Int. Ed. Engl.* 57 (2018) 172–176.
- Y. Zheng, Y. Jiao, Y. Zhu, L.H. Li, Y. Han, Y. Chen, A. Du, M. Jaroniec, S.Z. Qiao, Hydrogen evolution by a metal-free electrocatalyst, *Nat. Commun.* 5 (2014) 3783.
- S. Wang, L. Pan, J.-J. Song, W. Mi, J.-J. Zou, L. Wang, X. Zhang, Titanium-defected undoped anatase  $\text{TiO}_2$  with p-type conductivity, room-temperature ferromagnetism, and remarkable photocatalytic performance, *J. Am. Chem. Soc.* 137 (2015) 2975–2983.
- J.K. Nørskov, T. Bligaard, A. Logadottir, J.R. Kitchin, J.G. Chen, S. Pandelov, U. Stimming, Trends in the exchange current for hydrogen evolution, *J.*

Electrochem. Soc. 152 (2005) J23–J26.

[37] M. Zhu, S. Kim, L. Mao, M. Fujitsuka, J. Zhang, X. Wang, T. Majima, Metal-free photocatalyst for H<sub>2</sub> evolution in visible to near-infrared region: Black phosphorus/graphitic carbon nitride, J. Am. Chem. Soc. 139 (2017) 13234–13242.

[38] Z.-F. Huang, J. Song, X. Wang, L. Pan, K. Li, X. Zhang, L. Wang, J.-J. Zou, Switching charge transfer of C<sub>3</sub>N<sub>4</sub>/W<sub>18</sub>O<sub>49</sub> from type-II to Z-scheme by interfacial band bending for highly efficient photocatalytic hydrogen evolution, Nano Energy 40 (2017) 308–316.

[39] H. Yu, L. Shang, T. Bian, R. Shi, G.I.N. Waterhouse, Y. Zhao, C. Zhou, L.-Z. Wu, C.-H. Tung, T. Zhang, Nitrogen-doped porous carbon nanosheets templated from g-C<sub>3</sub>N<sub>4</sub> as metal-free electrocatalysts for efficient oxygen reduction reaction, Adv. Mater. 28 (2016) 5080–5086.

[40] J.-W. Zhang, S. Gong, N. Mahmood, L. Pan, X. Zhang, J.-J. Zou, Oxygen-doped nanoporous carbon nitride via water-based homogeneous supramolecular assembly for photocatalytic hydrogen evolution, Appl. Catal. B 221 (2018) 9–16.

[41] J. Fu, J. Yu, C. Jiang, B. Cheng, g-C<sub>3</sub>N<sub>4</sub>-based heterostructured photocatalysts, Adv. Energy Mater. 8 (2017) 1701503.

[42] L. Shi, K. Chang, H. Zhang, X. Hai, L. Yang, T. Wang, J. Ye, Drastic enhancement of photocatalytic activities over phosphoric acid protonated porous g-C<sub>3</sub>N<sub>4</sub> nanosheets under visible light, Small 12 (2016) 4431–4439.

[43] S. Jin, Are metal chalcogenides, nitrides, and phosphides oxygen evolution catalysts or bifunctional catalysts? ACS Energy Lett. 2 (2017) 1937–1938.

[44] A. Śliśarczyk, Z. Paszkiewicz, C. Paluszakiewicz, FTIR and XRD evaluation of carbonated hydroxyapatite powders synthesized by wet methods, J. Mol. Struct. 744 (2005) 657–661.

[45] Z. Zhang, J. Huang, Y. Fang, M. Zhang, K. Liu, B. Dong, A nonmetal plasmonic Z-scheme photocatalyst with UV- to NIR- driven photocatalytic protons reduction, Adv. Mater. 29 (2017) 1606688.

[46] J. Yu, Y. Hai, B. Cheng, Enhanced photocatalytic H<sub>2</sub>-production activity of TiO<sub>2</sub> by Ni(OH)<sub>2</sub> cluster modification, J. Phys. Chem. C 115 (2011) 4953–4958.

[47] A. Indra, A. Acharjya, P.W. Menezes, C. Merschjann, D. Hollmann, M. Schwarze, M. Aktas, A. Friedrich, S. Lochbrunner, A. Thomas, M. Driess, Boosting visible-light-driven photocatalytic hydrogen evolution with an integrated nickel phosphide–carbon nitride system, Angew. Chem. Int. Ed. Engl. 56 (2017) 1653–1657.

[48] P. Ye, X. Liu, J. Iocozzia, Y. Yuan, L. Gu, G. Xu, Z. Lin, A highly stable non-noble metal Ni<sub>2</sub>P co-catalyst for increased H<sub>2</sub> generation by g-C<sub>3</sub>N<sub>4</sub> under visible light irradiation, J. Mater. Chem. A 5 (2017) 8493–8498.

[49] Y. Xin, J.-G. Liu, Y. Zhou, W. Liu, J. Gao, Y. Xie, Y. Yin, Z. Zou, Preparation and characterization of Pt supported on graphene with enhanced electrocatalytic activity in fuel cell, J. Power Sources 196 (2011) 1012–1018.

[50] Y.H. Li, J. Xing, Z.J. Chen, Z. Li, F. Tian, L.R. Zheng, H.F. Wang, P. Hu, H.J. Zhao, H.G. Yang, Unidirectional suppression of hydrogen oxidation on oxidized platinum clusters, Nat. Commun. 4 (2013) 2500.

[51] D.J. Martin, K. Qiu, S.A. Shevlin, A.D. Handoko, X. Chen, Z. Guo, J. Tang, Highly efficient photocatalytic H<sub>2</sub> evolution from water using visible light and structure-controlled graphitic carbon nitride, Angew. Chem. Int. Ed. Engl. 53 (2014) 9240–9245.

[52] R. Abe, K. Sayama, K. Domen, H. Arakawa, A new type of water splitting system composed of two different TiO<sub>2</sub> photocatalysts (anatase, rutile) and a IO<sub>3</sub><sup>–</sup>/I<sup>–</sup> shuttle redox mediator, Chem. Phys. Lett. 344 (2001) 339–344.

[53] J. Tang, J.R. Durrant, D.R. Klug, Mechanism of photocatalytic water splitting in TiO<sub>2</sub>: Reaction of water with photoholes, importance of charge carrier dynamics, and evidence for four-hole chemistry, J. Am. Chem. Soc. 130 (2008) 13885–13891.